Int J Adv Manuf Technol (2013) 66:469–479
DOI 10.1007/s00170-012-4342-6

ORIGINAL ARTICLE

Strength and microstructure of laser fusion-welded Ti–SS dissimilar material pair

Gen Satoh · Y. Lawrence Yao · Caian Qiu

Received: 8 March 2012 / Accepted: 21 June 2012 / Published online: 4 July 2012

Abstract The ability to efficiently create robust and reliable dissimilar metal joints has the potential to enable new functionalities and reduce the manufacturing costs of medical devices. The need for dissimilar material welds in the medical device industry is driven by the unique properties exhibited by biocompatible materials such as stainless steel and titanium, as well as shape memory materials such as NiTi. Many material pairs, however, suffer from significant intermetallic phase formation during welding which greatly reduces their strength. This study investigates the microstructures and strength of the laser fusion-welded titanium–stainless steel dissimilar material pair as a simplified model of the NiTi–stainless steel pair. Compositional and structural analysis of the weld pool is performed and fracture morphologies are analyzed in different regions of the weld joint. The role of weld pool geometry, heat flow, and quench rate on the resultant phases, microstructures, and strength of the welds is discussed.

Keywords Laser welding · Dissimilar material welding · Stainless steel · Titanium · Intermetallic

1 Introduction

Joining of dissimilar materials is performed in order to take advantage of specific attributes of each material to enhance the performance of a product or introduce new functionalities. The need to join two different materials typically arises when one possesses an attribute that is required for functionality of the device but also has some inherent disadvantages such as increased cost or weight and thus cannot be used extensively. Some attributes of interest are corrosion resistance and biocompatibility, thermal and electrical properties, as well as mechanical properties such as Young's modulus and hardness. In the case where one material is a smart material such as a shape memory alloy, specific attributes such as superelasticity or the shape memory effect may also be exploited.

A number of dissimilar material joints have been successfully formed using various methods from fusion welding to diffusion bonding including metal–metal, metal–ceramic, and metal–polymer joints [1]. Materials with good compatibility such as Cu and Ni can be joined using fusion processes while pairs that form phases with undesirable properties upon mixing are typically joined in the solid state [2] or with the aid of a non-reactive interlayer [3, 4]. Dissimilar metal welding of the biocompatible materials stainless steel (SS) and the shape memory alloy nickel–titanium (NiTi) is of particular interest within the bio-medical industry due to the exceptional mechanical properties of NiTi and the low cost of stainless steel 316. This particular material pair, however, suffers from significant intermetallic formation after mixing which results in brittle joints which are unable to withstand handling and use [5]. A number of intermetallic phases exist even in the simplified binary Fe–Ti system as shown in Fig. 1 [6]. The addition of alloying elements such as Cr and Ni found in SS and NiTi introduces further complexities in microstructure and phase formation. The dissimilar material pair between stainless steel and titanium alleviates some of these complexities by reducing the nickel composition from roughly 50 at% in the NiTi to only ~10 at% in the SS while still enabling the formation of Ti–Fe-based intermetallics.

G. Satoh (✉) · Y. L. Yao
Department of Mechanical Engineering, Columbia University, New York, NY, USA
e-mail: gs2358@columbia.edu

C. Qiu
Champaign Simulation Center, Caterpillar, Champaign, IL, USA

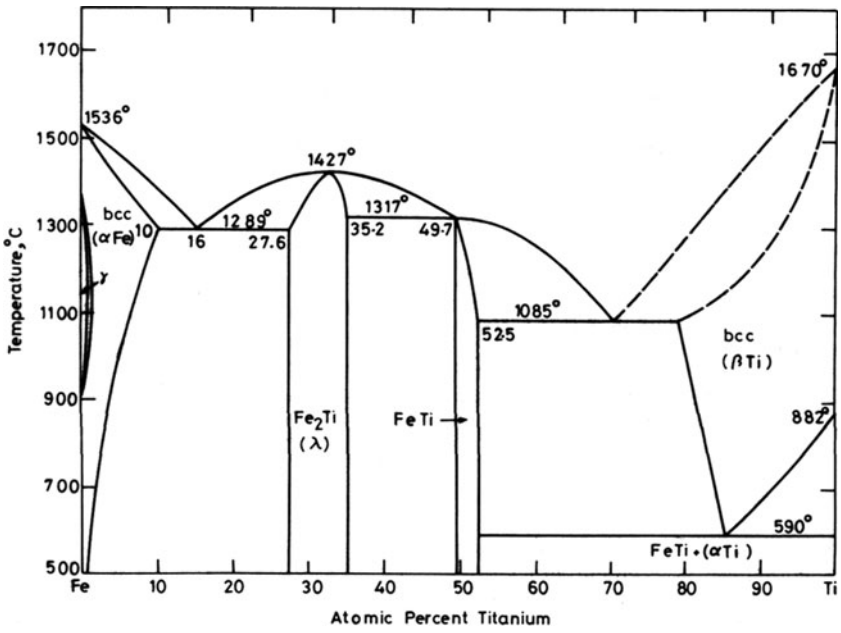

Fig. 1 Fe–Ti binary phase diagram showing existence of at least two intermetallic phases in the stainless steel–nickel titanium material pair [6]

Traditional joining methods such as arc welding when applied to dissimilar material pairs have been found to introduce excessive amounts of heat resulting in the formation of large volumes of intermetallics [7]. Some success has been found through the use of laser welding due to its precise, localized heat input capabilities which allows for small heat-affected zones, however, the joints still suffer from brittle intermetallic formation [8]. Li et al. have used laser brazing to join NiTi and SS through the use of silver-based filler materials; however, the addition of filler materials during welding adds significant complexity to the process and the filler material is not able to achieve corrosion resistances comparable to the base materials [9]. Diffusion bonding, where two materials are pushed together at high pressure and temperature in the solid state for extended periods of time to form a bond, has shown some success but requires strict tolerances on surface flatness, significant time, and the ability to impart large stresses on the materials [10]. These requirements are increasingly difficult to achieve as devices are created at small length scales as found within bio-medical devices. Ultrasonic welding, which uses pressure and high-frequency vibrations to create solid-state joints, has been shown to produce strong welds in a number of dissimilar metal pairs but is limited to lap joints and can be difficult to perform on thick sections and on strong and hard materials such as Ti [11]. A robust fusion welding process for the NiTi–SS pair would allow for reliable and efficient formation of strong joints for bio-medical applications. The development of such a process requires comprehensive understanding of the microstructures and failure mechanisms observed in this material pair in the fusion welding regime.

In this study, the use of pulsed laser welding to join titanium to SS 316 is investigated through the use of energy-dispersive x-ray spectroscopy (EDX) and electron backscatter diffraction (EBSD) for compositional and microstructural analysis. Fracture surface analysis is performed through scanning electron microscopy and EDX. Computational thermodynamics techniques are used to model phase evolution during solidification of multi-component systems.

2 Background

2.1 Equilibrium phases

The SS–Ti pair, while attractive for many applications, is not widely used due to the existence of multiple brittle intermetallics within the Fe–Ti phase diagram. Stainless steel, with a composition primarily consisting of Fe, Cr, and Ni, will form many of the same phases when combined with Ti as observed in the Fe–Ti material pair and thus suffers from many of the same issues with regards to mechanical strength and ductility. Figure 1 is a binary phase diagram containing the two main components expected in an SS–Ti dissimilar material weld, Fe and Ti [6]. While ternary Fe–Ti–Cr and Fe–Ti–Ni phase diagrams are available, the phases formed differ very little from the binary diagram at the Cr and Ni compositions found in SS. Phases omitted in the binary diagram are $NiTi_2$ and $TiCr_2$, which are expected to form in small amounts in an SS–Ti mixture. On the binary phase diagram a few phases

are formed, namely α-Ti, β-Ti, FeTi, λ, and α-Fe, in order of increasing Fe content.

In this case, λ represents $TiFe_2$ which has a C14 hexagonal Laves intermetallic structure. In the ternary Fe–Ti–Cr phase diagram, λ represents a solid solution of $TiFe_2$ and $TiCr_2$. The λ-Laves phase is close packed and has a homogeneity range between 64.8 and 72.4 at% Fe. β-Ti has a base-centered cubic (BCC) structure which at equilibrium will transform to α-Ti and TiFe through a eutectoid reaction. The intermetallic FeTi also has a BCC structure and only exists between 47.5 and 50.2 at% Fe. α-Fe also has a BCC structure.

2.2 Eutectic solidification

As can be seen in Fig. 1, a eutectic reaction occurs on the Ti-rich side with the formation of β-Ti and TiFe from liquid. At equilibrium, the formation of these two phases is typically in a lamellar structure with alternating β-Ti and TiFe plates. The microstructure is divided into colonies within which each set of plates has the same crystal orientation and a specific orientation relationship that aims to minimize the interfacial energy between the two phases. At higher cooling rates directionality is observed in the growth of the plates resulting in an oriented microstructure with the plates aligned in the direction of heat flow.

It has been shown by Yu et al. that during solidification of near-eutectic compositions in the Ti–Fe pair, a supersaturated β-Ti(Fe) solid solution will form first followed by the FeTi intermetallic phase [12]. Dendrites in this material pair are typically in the form of TiFe dendrites within a supersaturated β-Ti(Fe) matrix. As with other eutectic structures solidified under a thermal gradient, the dendrites will form preferentially in the direction of heat flow. While it has been shown by Louzguine-Luzgin et al., that the interfaces between coarse TiFe dendrites and the matrix cause crack propagation to be arrested [13], the formation of a directional dendritic structure introduces a great deal of anisotropy to the mechanical properties of the material which typically show significantly more robust mechanical properties along the dendrite growth direction and limited strength in the transverse direction.

While strict observation of the equilibrium phase diagram (Fig. 1) suggests that α-Ti, the hexagonal close-packed (HCP)-structured Ti phase, should form below 595 °C, it has been shown that a number of factors can stabilize the β-phase. One of the strongest effects comes from alloying. A number of elements such as Mo, V, W, Nb, Ta, Fe, and Cr have been shown to be β-stabilizers meaning that their existence lowers the α/β transus. Still other elements such as Al and O are α-stabilizers and have the opposite effect. The overall effect of these elements in captured by calculating the %Mo-equivalent composition which is written as [14]

$$\begin{aligned}\%\text{Mo Equivalent} = {} & 1.0(\%\text{Mo}) + 0.67(\%\text{V}) \\ & +0.44(\%(\text{W}) + 0.28(\%\text{Nb}) + 0.22(\%\text{Ta}) \\ & +2.9(\%\text{Fe}) + 1.6(\%\text{Cr}) - 1.0(\%\text{Al})\end{aligned} \quad (1)$$

It is suggested that for %Mo-equivalent values exceeding 10 %, a β-alloy will form. In the Ti–Fe pair, only a small amount of mixing is required to exceed the 10 % Mo-equivalent threshold. In addition to compositional changes that stabilize the β-phase, extended solubility of Fe in β-Ti has also been observed at high cooling rates [15]. This allows for the formation of single-phase β-Ti(Fe) at compositions outside the equilibrium homogeneity range.

2.3 Numerical modeling

While binary and ternary phase diagrams are useful for understanding the effects of the two or three main alloy components on the phases formed during welding, they are unable to take into account any more than three components. In order to account for the effects of larger numbers of components, computational thermodynamics techniques are often used. The basis for phase prediction using computational thermodynamics is the calculation of the free energies of different phases in a material as a function of temperature, T; pressure, P; and composition, X. For a mechanical mixture between two pure components the free energy can be written as [16]

$$G^M = X_A H_A + X_B H_B - T(X_A S_A + X_B S_B) \quad (2)$$

Where X_i are the mole fractions, H_i are the enthalpies, and S_i are the entropies of the pure components A and B. If, however, a solution is created, the free energy is written as

$$G^S = X_A \overline{H}_A + X_B \overline{H}_B - T\left(X_A \overline{S}_A + X_B \overline{S}_B\right) - T\Delta S_M \quad (3)$$

Where barred quantities indicate values when in solution and ΔS_M is the entropy of mixing which accounts for the configurational entropy of the solution. For dilute solutions, the configurational entropy can be written as

$$\Delta S_M = -R(X_A \ln X_A + X_B \ln X_B) \quad (4)$$

For non-ideal solutions where properties in the solution and in pure form are different, the free energy is written as

$$\begin{aligned} G^S &= G^M + X_A\left(\overline{H}_A - H_A\right) \\ &+ X_B\left(\overline{H}_B - H_B\right) \\ &- T\left[X_A\left(\overline{S}_A - S_A\right) + X_B\left(\overline{S}_B - S_B\right)\right] \\ &+ RT(X_A \ln X_A + X_B \ln X_B) \\ &= G^M + \Delta H^{xs} - T\Delta S^{xs} - T\Delta S_M \end{aligned} \quad (5)$$

Where *xs* quantities are the difference of the value relative to an ideal solution.

Equation 5 thus represents the free energy of a specific phase as a function of temperature and composition with pressure typically held constant. Once these relationships are known for each phase in the material, an equilibrium phase diagram can be created by plotting the phase which has the lowest free energy at each composition and temperature. This is the basis of the CALPHAD (CALculation of PHAse Diagrams) method.

In order to extend these equations past binary combinations to higher-order systems, extra terms are added for each new component and higher-order free-energy "surfaces" are plotted rather than curves. In this study, these relationships are calculated using THERMOCALC [17]. In this study the TCFE2 THERMOCALC database is used in order to capture the phases formed in stainless steel-titanium mixtures. Each material database includes polynomials which describe the Gibbs free energy of individual phases in a system as a function of temperature and composition and are developed with the aid of experimental information as well as Gibbs energy models [17]. By determining the phases with the lowest free energies at different temperature/composition values, multi-component phase diagrams can be calculated. In addition, the equilibrium phase evolution during solidification of a material can be determined as a function of temperature.

3 Experimental setup

Titanium grade 2 (HCP α-phase) and Stainless Steel 316 (FCC γ-phase) coupons measuring 50×36×0.8 mm were sectioned from rolled sheets. The surfaces of the samples were sanded with aluminum oxide abrasive pads with an equivalent grit of roughly 100 to remove impurities and dull any polished surfaces and cleaned with acetone immediately prior to welding. Welds were performed in a butt-weld geometry with the SS coupon clamped in a fixture and the Ti coupon placed next to it with no gap. The lack of a gap between the plates and free movement of the Ti coupon limits the thermal stresses induced by the welding process [18]. The samples were welded using a pulsed Nd:YAG laser at a wavelength of 1,064 nm and a maximum average power of 2 kW. The diameter of the Gaussian laser spot on the sample surface was 1 mm. Laser pulses were produced at controlled repetition rate of 100 Hz, each with a rectangular temporal pulse profile. A six-axis robotic arm with an end effector was used for positioning and translation at a constant speed of 20 mm/s to achieve constant pulse overlaps. Additionally, ultra-high-purity Argon gas was used to shield the weld pool from atmospheric contamination along the top and bottom surfaces of the weld. A schematic diagram of the process is shown in Fig. 2.

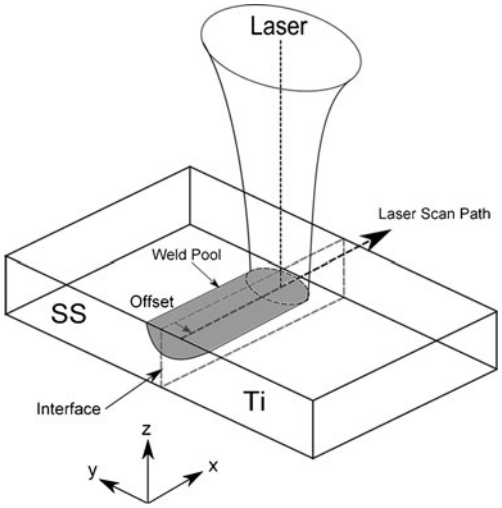

Fig. 2 Schematic diagram of welding geometry. Note offset of laser beam from interface toward Ti sample

Processing parameters were chosen using a three-level, three-factor design of experiment array. The three factors analyzed were the laser beam offset from the SS–Ti interface, pulse duration, and average power. Samples were processed at offsets of 0, 150, and 300 μm from the SS–Ti interface toward the Ti plate, pulse durations of ~2.5, 3.6, and 6.5 ms, and average powers of 300, 525, and 750 W. For a constant average power and repetition rate, changes in the pulse duration were accompanied by changes in the peak power in order to maintain constant pulse energy. Welded samples were sectioned using wire electrical discharge machining into small samples for cross-section analysis as well as dog-bone samples for tensile testing. The dog-bone samples were cut to sub-size specimen specifications as defined in ASTM standard #E8-09 [19].

Samples for cross-sectional analysis were ground using carbide paper and then polished using alumina slurries. After polishing, the titanium was etched using Kroll's reagent while the stainless steel was etched using a mixture of nitric acid, hydrofluoric acid, and water. Compositional analysis was performed using EDX and crystal structure analysis was performed using EBSD. Surface morphologies were observed using a scanning electron microscope (SEM) and tensile testing was performed using a uniaxial tensile testing machine operating at a cross-head speed of 0.1 mm/min.

4 Results and discussion

4.1 Weld geometry

Figure 3 is a typical weld cross-section (*yz*-plane) for samples processed at an average power of 750 W. The weld pool

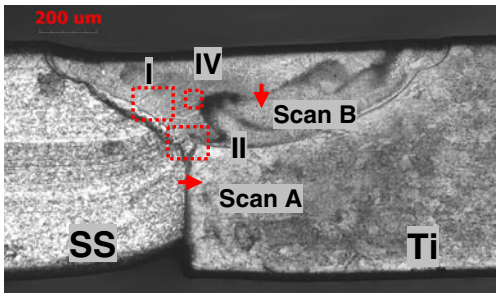

Fig. 3 Typical weld cross-section (*yz*-plane). Note asymmetry of weld pool and existence of various microstructures within weld pool. Laser power: 750 W, offset 300 μm, pulse width: 3.7 ms, scan speed: 20 mm/s

is observed to be confined to the upper portion of the plates and some variation in symmetry about the original SS–Ti interface was observed for different laser offsets as expected due to the large differences in material properties across the weld interface. The thermal diffusivity for Ti, 6.9e−6 m^2/s, is almost twice that of SS, 4.08e−6 m^2/s, and Ti also has a higher melting temperature, 1,665 versus 1,375 °C. This requires a greater amount of heat to be supplied to the Ti in order to ensure it reaches its melting temperature which is achieved through the offset of the laser beam toward the Ti. Samples processed at high powers show greater penetration and weld size compared to lower powers. The weld cross-section, however, shows that the main weld pool does not reach the bottom of the plates even for the highest power welds. The aspect ratio achieved by these welds indicates a fusion mechanism rather than a keyhole weld which limits the penetration achievable. The top weld surface as observed from the cross-section in Fig. 3 is flat and nearly flush with the base Ti and SS plates. The minimal gap between the plates and lack of filler material results in weld pools without any buildup above the surface of the original plates. This surface morphology is typical of welds performed in the conduction welding regime.

4.2 Weld strength

Fracture stress values for samples processed at an average power of 750 W with various offsets and pulse durations are shown in Table 1. Load-extension curves acquired during tensile testing showed no evidence of appreciable plastic deformation and no necking was observed suggesting primarily brittle fracture of the weld joints. Samples processed at the highest average power, 750 W, were chosen for analysis in this study due to their greater penetration depth. All samples processed at this power fractured at the weld joint rather than in the base material and fracture occurred closer to the SS side of the weld zone. Fracture stress values were calculated using the maximum load observed during tensile testing and the fracture surface area (*xz*-plane)

Table 1 Failure stresses from tensile tests

Condition	Offset (μm)	Pulse duration (ms)	Failure stress (MPa)
1	0	6.5	81.4±72.5
2	150	6.5	41.1±12.0
3	300	6.5	–
4	0	3.6	65.1±2.8
5	150	3.7	–
6	300	3.7	81.0±64.1
7	0	2.5	–
8	150	2.5	–
9	300	2.5	–

Note large variance in strength. Samples with no stress value fractured upon solidification

observed under optical microscopy. The fracture stress values reported in Table 1 show that the weld joints are weaker than the base metal even when considering their smaller cross-sectional area and have a great deal of scatter between samples. The strongest samples were able to achieve a failure stress that was ~60 % of the yield stress of stainless steel and ~35 % of the ultimate tensile strength of titanium. Ideally, the weld itself should be stronger than the base material and in the case of dissimilar material welds, should be stronger than the weaker of the two materials being joined. Thus, these initial results suggest that further understanding of the microstructure and failure mechanisms in stainless steel to titanium dissimilar material welds is required to form joints of adequate strength.

The lack of necking during tensile testing of the welds along with the large scatter in tensile strengths show high sensitivity to initial cracks within the weld and again suggests that brittle fracture is the main failure mode. Audible cracking was noted during cooling of the welds after solidification which varied in degree for different processing parameters. Samples processed at the shortest pulse duration of ~2.5 ms and thus the highest peak power are not included in Table 1 due to extensive cracking of the weld during cooling resulting in failure of the joints. Cracks similar to those shown in the cross-section in Fig. 11 were observed in the weld zone for a number of laser parameters and were typically oriented perpendicular to the laser scanning direction on the *yz*-plane and are likely caused by the difference in the coefficients of thermal expansion between the SS, ~16e−6 m/m/°C, and Ti, ~9e−6 m/m/°C. After the laser passes, assuming the two materials are initially at the same temperature, the stainless steel will undergo a greater degree of contraction than the titanium during cooling. Since the two materials are joined, this discrepancy leads to the formation of tensile stresses and cracks in the SS side and compressive stresses in the Ti side of the weld.

4.3 Weld pool microstructure and composition

To understand the cause of the low joint strength and high variability microstructural analysis was performed on the joints. Several different microstructures are observed in the weld pool in Fig. 3. A distinct layer lines the SS–weld pool interface, passing through the lower left corner of region I, while further into the melt pool on the SS side, a coarse dendrite-like morphology is observed which extends across the top of the weld pool toward the Ti side. The majority of the Ti side of the weld pool shows a finer microstructure. Some indication of joining below the weld zone is seen as well in region II of the image. Figure 4 shows higher magnification optical micrographs of two sections outlined in Fig. 3. Dendrites are clearly observed in Fig. 4a, along with a layer separating them from the base stainless steel. The existence of dendrites oriented primarily normal to the solid–liquid interface indicates directional solidification from the interface toward the center of the weld pool. Figure 4b shows the area below the main weld pool and a thin melt zone between the two sheets is observed. Since welds performed in this study are within the conduction welding mode, this joining below the main weld pool is considered to be caused by heat accumulation at the interface resulting in localized melting of the materials or weld pool flow along the interface.

Figure 5 shows an EDX line scan across scan B as depicted in Fig. 3. While the average compositions across the coarse/fine microstructure boundary are nearly identical, the coarse dendrite structure shows significantly more variation in the composition. The average composition of ~70 at% Ti, ~20 at% Fe, and ~3 at% Cr in addition to small amounts of Ni, Mo, and Mn when considered in the context of the binary Fe–Ti phase diagram suggests formation of a β-Ti/FeTi eutectic. Figure 6 shows the composition profile across dendrites in the coarse dendrite region toward the SS side of the weld pool. Clear differentiation between the dendrite and interdendritic regions is observed in Fig. 6a with the Ti and Fe compositions moving in opposite directions. The average composition of the Ti-rich regions (interdendritic regions) is ~75 at% Ti and ~18 at% Fe with the remainder being taken up by components such as Mo and Cr. The dendritic regions have a more balanced composition with the Ti composition nearing ~50 at% and the Fe composition nearing ~40 at%. While these two compositions are different from those expected during equilibrium eutectic solidification, it has been shown that rapid solidification will cause extended solubility in β-Ti and TiFe [15]. Thus, initial compositional analysis suggests that the dendrites are TiFe and the interdendritic regions are supersaturated β-Ti.

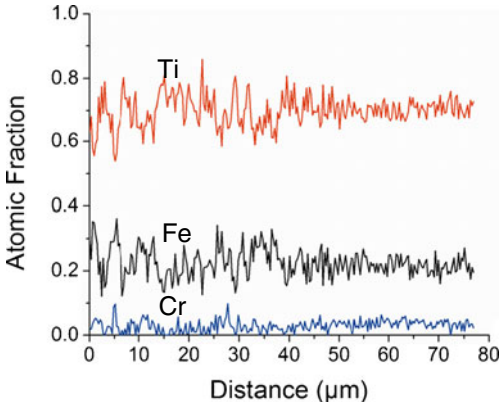

Fig. 5 EDX line scan across SS–Ti interface (*scan B* in Fig. 3). Note difference in composition uniformity across interface

An EBSD surface map of a region containing a coarse dendritic microstructure (region IV in Fig. 3) is shown in Fig. 7. The Euler angle map shown in Fig. 7b shows large regions with similar dendrite growth directions as having the same orientation. These areas include the darker interdendritic regions as well. Each of these regions with the same crystal orientation are considered to be eutectic colonies. Both the dendritic and interdendritic regions show a BCC structure which when considered in terms of the equilibrium phase diagrams suggests a β-Ti/FeTi mixture. The composition of these dendrites and their interdendrite regions were shown to be close to TiFe and β-Ti, respectively. Both of these phases have a BCC crystal structure. The observation of BCC structure through EBSD is further evidence that these structures are in fact TiFe dendrites in a supersaturated β-Ti matrix.

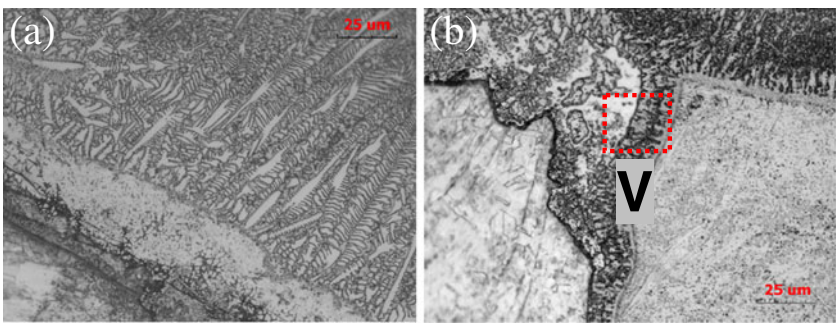

Fig. 4 Optical micrographs of regions **a** *I* and **b** *II* from Fig. 3. Note coarse dendritic structure in region I and joining in the form of a thin molten layer in region II

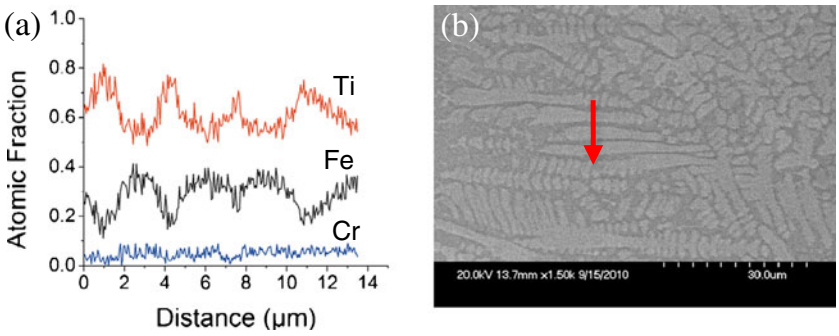

Fig. 6 EDX line scan across coarse dendrites observed on cross-section (*yz*-plane). Note higher Ti content in interdendrite regions

A line scan EDX profile across the lower portion of the weld interface (scan A in Fig. 3) is shown in Fig. 8 and clearly shows the existence of a mixed layer at the interface with a composition between that of pure SS and pure Ti. The composition abruptly changes at the SS interface while the transition is more gradual on the Ti side of the joint. This is due to the higher diffusivity of Fe and Cr into Ti than Ti into SS [20]. When Fe and Cr diffuse into the Ti side of the joint, they will be dissolved into Ti to form a solid solution. This solution layer adjacent to the Ti has a gradual variation in Fe content. With further diffusion of Fe, it will reach its solubility limit in Ti, and then the compound FeTi will start to form according to the Fe–Ti phase diagram in Fig. 1. Since diffusion occurred between the multi-component alloy SS and pure Ti, a pure FeTi layer would not be formed. Instead, a mixture of FeTi and Ti-based solid solution will be produced. The mixed zone is observed to also have a similar composition to that observed in the dendritic regions of the weld pool as discussed above. This again suggests a mixture of FeTi and β-Ti in this region; however, no significant fluctuations in composition are observed across the interface or along the interface in the *z*-direction (not shown). If FeTi regions were to exist in this region, a similar profile to that observed in Fig. 6 would be expected. As discussed above, extended solubility of Fe in the β-Ti structure has been shown to occur for high cooling rates such as those experienced during laser welding [15]; however within the main weld pool, dendrites of TiFe were seen to form. Thus, the cooling rate in the lower section of the weld must be significantly higher such that a single-phase region is formed from a eutectic composition. This high cooling rate is likely due to the thin film-like geometry of the molten zone with a thickness of roughly 4 μm. The large surface area connecting the molten material to the surrounding solid on both sides of the interface and the limited volume of molten material would allow for a significant increase in the cooling rate within this region and the formation of non-equilibrium microstructures and phases.

Figure 9 shows EBSD scans of an area where a layered structure is observed in the weld pool (region V in Fig. 4b). The lighter-colored region on the left of Fig. 9a was determined by EDX to be a nearly equiatomic Ti–Fe layer and the darker colored region a ~70 at% Ti layer that extends from the bottom of the main melt pool toward the bottom of the joint. Figure 9b is a structure map of the same region with BCC-structured regions colored red and HCP-structured regions colored green. The layer closer to the SS side of the weld exhibits an HCP structure while the layer closer to the Ti side of the weld shows a BCC structure. The BCC structure, along with the homogeneous composition of roughly 70 at% Ti and 20 at% Fe suggests that this layer is comprised of β-Ti grains supersaturated with Fe. As discussed above, the adjacent HCP layer has a composition which, at equilibrium, would form a mixture of FeTi and $TiFe_2$ (λ-Laves). The observation of a hexagonal structure through EBSD suggests that this layer consists primarily of $TiFe_2$.

Phase development curves for materials with similar compositions to those observed in the aforementioned layers modeled using CALPHAD techniques are shown in

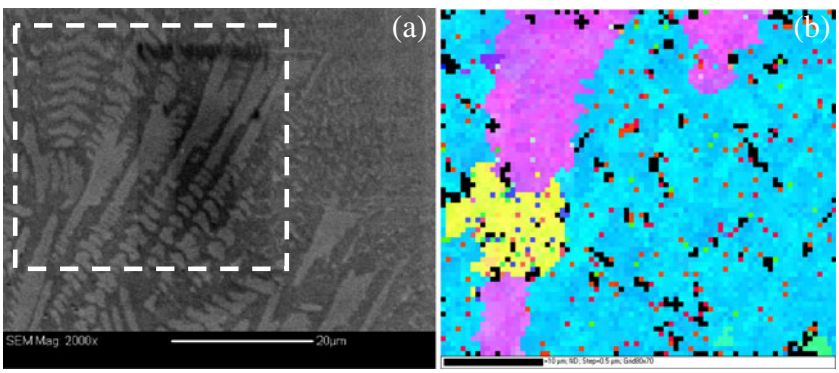

Fig. 7 EBSD scan of area IV in Fig. 3. **a** SEM scan showing dendritic structure and EBSD measured area (*outlined*). **b** Euler angle map of measured area from **a** showing various crystal orientations within eutectic colonies

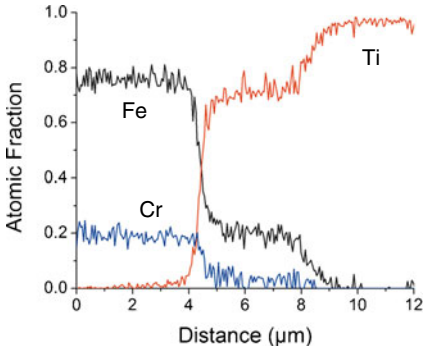

Fig. 8 EDX line scan across SS–Ti interface (*scan A* in Fig. 3). Note homogeneous composition within weld zone and significant diffusion of Fe and Cr into Ti

Fig. 10a, b. Figure 10a shows the mole fraction of phases present in a material with a composition of 18.19 % Fe, 74.00 % Ti, 4.53 % Cr, 1.38 % Ni, 1.66 % Mn, and 0.23 at% Mo, as a function of temperature. This composition is very similar to that observed in the Ti-rich interfacial layer as well as in the main weld pool as determined through EDX. The model suggests that the first phase to form at roughly 1250 °C is BCC or β-Ti. Once the temperature has reached ~900 °C the intermetallic phase, FeTi, starts to form. In the main weld pool a microstructure consisting of TiFe dendrites within a β-Ti matrix was observed. This phase mixture is consistent with that predicted by the CALPHAD model at this composition. The Ti-rich interfacial layer showed a BCC structure and a homogeneous Ti-rich composition. The lack of TiFe in this layer is considered to be due to the high quench rate experienced by the thin interfacial layer during solidification. As the model shows, even at equilibrium, the β-Ti begins to form at a temperature over 300 °C above FeTi. At high quench rates, it has been shown that TiFe may not have time to nucleate and grow resulting in a single-phase region near the eutectic composition [15].

Figure 10b shows the mole fraction of phases present in a material with a composition of 37.00 % Fe, 46.59 % Ti, 10.70 % Cr, 2.95 % Ni, 2.47 % Mn, and 0.29 at% Mo as a function of temperature. This composition is very similar to that observed in the near-equiatomic layer toward the SS side of the joint in Fig. 4b. The model predicts the initial

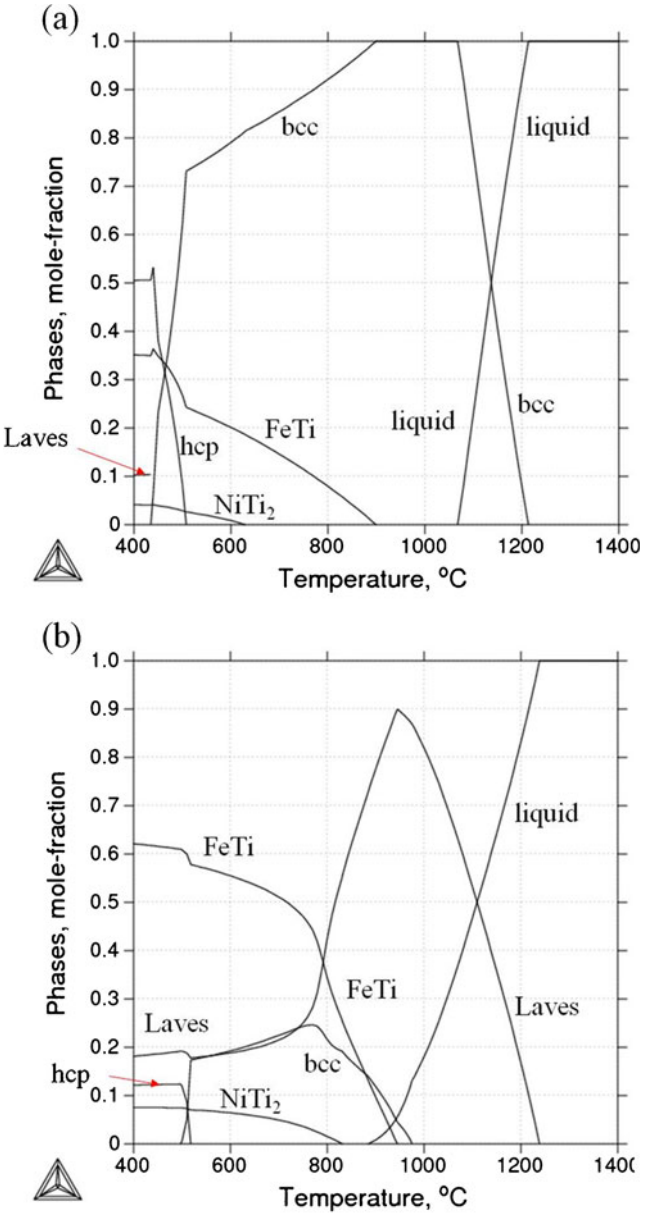

Fig. 10 Simulation results for mole fraction of phases for **a** 18.19 % Fe, 74.00 % Ti, 4.53 % Cr, 1.38 % Ni, 1.66 % Mn, and 0.23 at% Mo; and **b** 37.00 % Fe, 46.59 % Ti, 10.70 % Cr, 2.95 % Ni, 2.47 % Mn, and 0.29 at% Mo regions

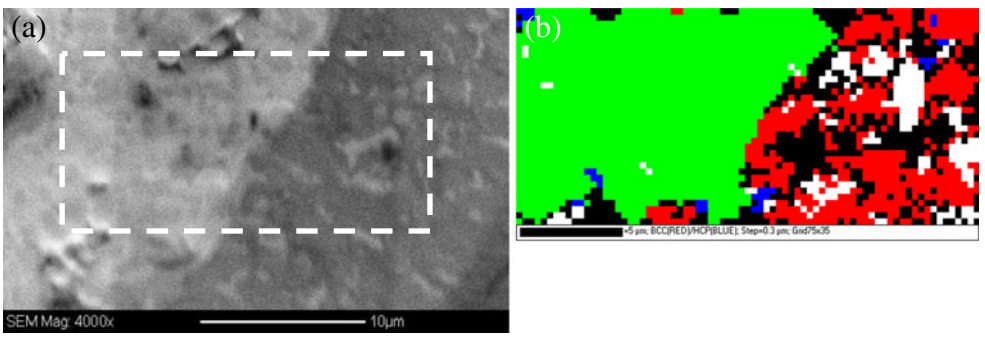

Fig. 9 EBSD scan of area V in Fig. 4b. **a** SEM scan showing layered structure as well as EBSD measured area (*outlined*). **b** Structure map of measured area with *red* indicating BCC and *green* indicating HCP structures

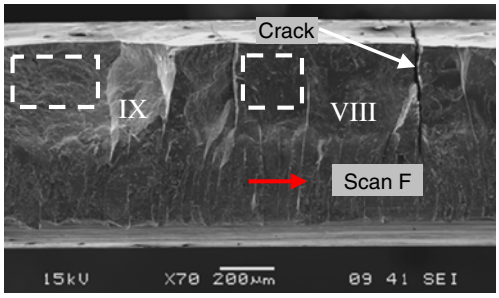

Fig. 11 Fracture surface (SS side, typical). Note different morphologies in *upper* and *lower sections*

formation of the Laves phase, $TiFe_2$ with FeTi forming at a temperature a few hundred degrees lower. Thus the existence of predominantly $TiFe_2$ in the near-equiatomic interfacial layer is consistent with the CALPHAD model and is likely due to the high quench rate in the lower weld zone. The material in this section does not have sufficient time for TiFe formation during solidification.

4.4 Fracture surface analysis

Fracture surfaces created during tensile testing of the welded samples were analyzed using SEM and EDX in order to determine the fracture mode and position of failure within the weld pool. As noted above, low-magnification observation of the fracture surfaces showed that fracture always occurred along the original SS–Ti interface position or toward the SS side of the weld pool. Figure 11 is an SEM image of a typical SS fracture surface (*xz*-plane). The brighter region toward the top of the image is the top surface of the weld (*xy*-plane). Cracks can be observed propagating in the *yz*-plane on the upper part of the weld joint and can be seen on the top surface of the weld as well. The lighter-colored region with the long horizontal lines at the bottom of the image is the unwelded portion of the plate. Figure 11 depicts significantly different fracture surfaces along the top and bottom halves of weld. The surface of the bottom half is punctuated by equally spaced lines oriented perpendicular to the laser scan direction. In contrast, the upper fracture surface consists of larger contiguous areas with more significant topographical changes.

Figure 12a shows a higher magnification SEM image of region VIII in the upper fracture surface. A large smooth region on the order of a few hundred micrometers tall is observed on the left of the image with a number of finger-like features observed on the right. The composition of this region as determined through EDX was ~70 at% Ti and ~20 at% Fe and was observed to be homogenous throughout. This overall composition is very close to that observed in the interdendritic regions of the main weld pool as shown in Fig. 6. EDX analysis of the corresponding Ti fracture surface showed a nearly identical composition. This suggests that fracture occurred within the interdendritic regions in the main weld pool rather than at the dendrite surfaces. As observed in Fig. 11, however, the entire upper fracture surface does not have this same smooth surface morphology. Figure 12b is a high-magnification SEM image of region IX in Fig. 11. The surface roughness is observed to be greater than region VIII and the composition is found to be much closer to the roughly 50 at% Ti and 35 at% Fe observed in the Laves-phase layer toward the SS side of the weld zone in Fig. 3. Regions with this rough fracture surface and low Ti content are found to consistently occur closer to the SS side of the weld pool than the smooth Ti-rich regions.

Fracture in the main weld zone of the material is thus observed to occur within two different regions of the weld pool, the first being the interdendritic zones in the coarse dendritic microstructure located toward the SS side of the weld pool and the second being the layer of Laves-phase lining the SS–weld pool interface. It is important to note that fracture surfaces originating in the coarse dendritic microstructure regions almost exclusively showed a smooth surface structure at high magnification and were always nearly perpendicular to the applied tensile load direction. This surface morphology and crack geometry suggests that all of these regions failed through interdendritic cracking between dendrites that were oriented nearly perpendicular to the loading direction. Fracture also occurs in the Laves-phase layer on the SS–weld pool interface which is oriented at an angle with respect to the applied tensile load. It is

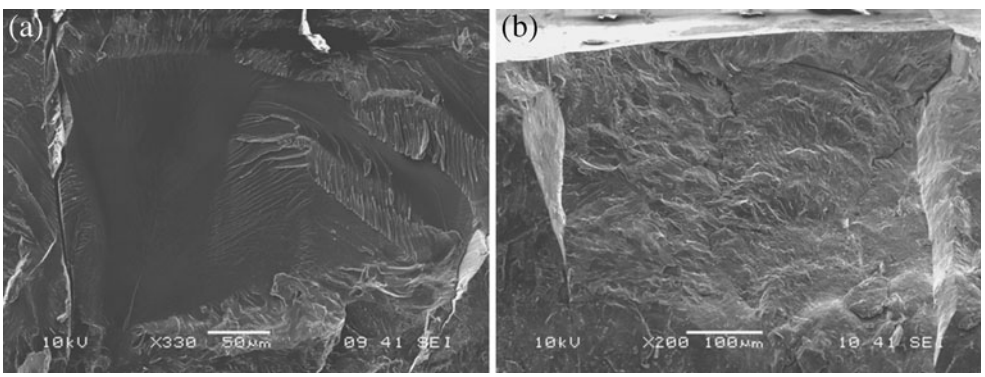

Fig. 12 SEM images of regions **a** *VIII* and **b** *IX* from Fig. 11. Note large, smooth fracture surface in region VIII and rough surface in region IX

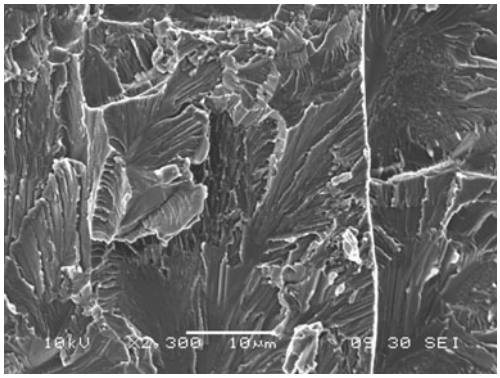

Fig. 13 SEM image of lower fracture surface in Fig. 11. Note vertically oriented cracks formed through grains and surface indicative of cleavage fracture

considered that in regions where fracture is observed in the Laves phase, the TiFe dendrites are primarily oriented parallel to the tensile loading direction resulting in greater strength.

A high-magnification SEM image of the lower fracture surface from Fig. 11 is shown in Fig. 13. The surface appears rougher than that observed in the interdendritic fracture surfaces in the main weld pool suggesting a different fracture mechanism is active in this region. Figure 14a is an EDX line scan performed across the lower interface in the *x*-direction (scan F in Fig. 11). The composition is seen to fluctuate significantly within this scan and small sections with the same composition are observed. Upon careful analysis, it is found that the composition changes at each vertical line is between Ti rich and Fe rich suggesting that either different phases are formed alternately along the *x*-direction or that there are height differences between the different sections.

Figure 14b is a topographical line profile obtained along scan F in Fig. 11 through optical profilometry. The profile shows significant topographic variation along the laser scan direction with a period very similar to that observed in the composition profile in Fig. 14a. The vertical lines observed in the SEM images are considered to be cracks in the *yz*-plane which separate regions located closer to the SS and Ti sides of the thin melt zone. This structure can be understood in the context of Fig. 8, the compositional profile across the lower weld pool interface. As discussed previously, the composition within the lower weld pool is homogeneous. The two main compositions observed on the lower fracture surface (Fig. 14a) are ~70 at% Ti/20 at% Fe and ~20 at% Ti/60 at% Fe. In Fig. 8, these two compositions occur at different locations. The ~70 at% Ti composition occurs across the entire weld pool while the ~60 at% Fe composition only occurs at the interface between the base SS and the weld pool. When considered in the context of Fig. 14b which shows a height difference between adjacent surfaces of roughly 8 μm which is on the order of the width of the lower weld pool, it is likely that fracture is occurring alternately on the SS–weld and Ti–weld interfaces. Movement of the crack between the SS–weld and Ti–weld interfaces may be due to cracks formed by thermal stresses during cooling of the dissimilar weld joint.

5 Conclusion

Laser fusion-welded dissimilar joints between stainless steel 316 and titanium grade 2 have been investigated as a simplified model for the NiTi—stainless steel dissimilar material pair. While joints between the two materials reaching roughly 60 % of the yield stress of stainless steel were formed, the variability in joint strengths and brittle nature of the welds were found to be limitations on the fusion welding of this dissimilar material pair. EDX and EBSD analysis indicated the formation of coarse intermetallic TiFe dendrites within a β-Ti matrix in the main weld pool and single-phase supersaturated β-Ti(Fe) of the same average composition in the lower weld zone. Fracture surface analysis shows that smooth interdendritic fracture between dendrites oriented perpendicular to the tensile load is the predominant mechanism of failure in the main weld pool, while alternating failure along the SS–weld and Ti–weld

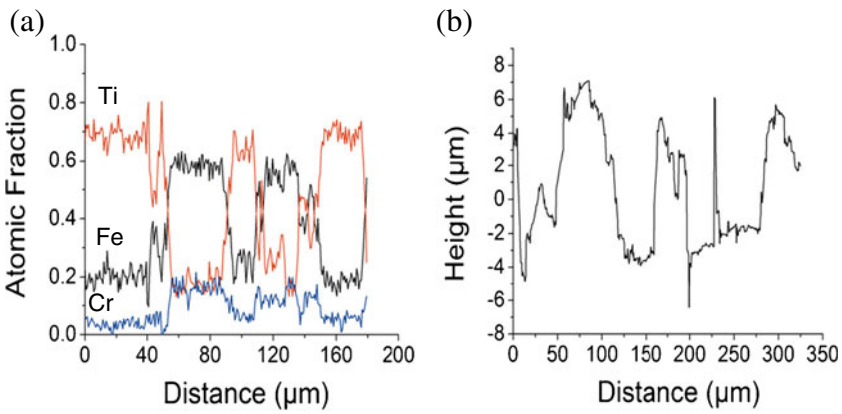

Fig. 14 **a** EDX composition profile and **b** topographic profile across lower fracture surface (*scan F* in Fig. 11). Abrupt changes in composition and height coincide with the periodic vertical crack-like features

interfaces was observed in the lower weld zone. Significantly greater surface area formation was observed in the lower portion of the weld suggesting that the single-phase supersaturated β-Ti(Fe) structure may be beneficial for fracture resistance. This non-equilibrium phase formed below the main weld pool where high cooling rates inhibited the growth of dendritic structures. Thus, further increasing the cooling rate experienced within the entire weld joint through decreases in weld pool size, greater heat localization, and external cooling is considered to be a promising approach for creating robust dissimilar metal welds between titanium and stainless steel.

Acknowledgment The authors would like to acknowledge Prof. James S. Im of the Materials Science Program in the Department of Applied Physics and Applied Mathematics at Columbia University and the Materials Research Science and Engineering Center, Columbia University for the use of their equipment.

Conflict of interest The authors declare that they have no conflict of interest.

References

1. Bauer I, Russek UA, Herfurth HJ, Witte R, Heinemann S, Newaz G, Mian A, Georgiev D, Auner GW (2004) "Laser microjoining of dissimilar and biocompatible materials," Proceedings of SPIE, pp. 454–464
2. Ghosh M, Chatterjee S (2005) Effect of interface microstructure on the bond strength of the diffusion welded joints between titanium and stainless steel. Mater Charact 54(4–5):327–337
3. Lee MK, Lee JG, Choi YH, Kim DW, Rhee CK, Lee YB, Hong SJ (2010) Interlayer engineering for dissimilar bonding of titanium to stainless steel. Mater Lett 64(9):1105–1108
4. Li M, Sun D, Qiu X, Liu J, Miao K, Wu W (2007) Effects of silver based filler metals on microstructure and properties of laser brazed joints between TiNi shape memory alloy and stainless steel. Sci Technol Weld Join 12(2):183–189
5. Ghosh M, Chatterjee S (2002) Characterization of transition joints of commercially pure titanium to 304 stainless steel. Mater Charact 48(5):393–399
6. Raghavan V (1987) Phase diagrams of ternay iron alloys. ASM International, Metals Park
7. Sun Z, Ion JC (1995) Review laser welding of dissimilar metal combinations. J Mater Sci 30:4205–4214
8. Vollertsen F, Grupp M (2005) Laser beam joining of dissimilar thin sheet materials. Steel Res Int 76(2):240–244
9. Li MG, Sun DQ, Qiu XM, Yin SQ (2006) Corrosion behavior of the laser-brazed joint of TiNi shape memory alloy and stainless steel in artificial saliva. Mater Sci Eng, A 441:271–277
10. Kundu S, Ghosh M, Laik A, Bhanumurthy K, Kale G, Chatterjee S (2005) Diffusion bonding of commercially pure titanium to 304 stainless steel using copper interlayer. Mater Sci Eng, A 407(1–2):154–160
11. Graff K (2005) New developments in advanced welding. Woodhead Publishing, Cambridge
12. Yu C, Wu MF, Lu H (2006) Factors influencing formation and growth of coarse Ti–Fe compound in Ti–Fe eutectic reaction. Sci Technol 11(3):265–271
13. Louzguine-Luzgin DV, Louzguina-Luzgina LV, Kato H, Inoue A (2005) Non-equilibrium Ti–Fe bulk alloys with ultra-high strength and enhanced ductility. Mater Res Soc Symp Proc 851:3–8
14. Polmear I (2005) Light alloys. Butterworth-Heinemann, Oxford
15. Ray R (1972) The constitution of metastable titanium-rich Ti–Fe alloys: an order–disorder transition. Metall Trans 126 (3):362–629
16. Gordon P (1983) Principles of phase diagrams in materials systems. Robert E. Krieger Publishing Company, Malabar
17. Jansson B (1993) The thermo calc project. Thermochim Acta 214 (1):93–96
18. Ely KJ (2001) Conduction welding, handbook of laser materials processing. Magnolia Publishing, Orlando, pp 354–357
19. ASTM (2009) Standard test methods for tension testing of metallic materials. ASTM International, West Conshohocken
20. Kale GB, Patil RV, Gawade PS (1998) Interdiffusion studies in titanium-304 stainless steel system. J Nucl Mater 257 (May):44–50